

Color Mapping Functions For HDR Panorama Imaging: Weighted Histogram Averaging

Yilun Xu, Zhengguo Li, *Senior Member, IEEE*, Weihai Chen*, *Member, IEEE*, and Changyun Wen, *Fellow, IEEE*

Abstract—It is challenging to stitch multiple images with different exposures due to possible color distortion and loss of details in the brightest and darkest regions of input images. In this paper, a novel color mapping algorithm is first proposed by introducing a new concept of weighted histogram averaging (WHA). The proposed WHA algorithm leverages the correspondence between the histogram bins of two images which are built up by using the non-decreasing property of the color mapping functions (CMFs). The WHA algorithm is then adopted to synthesize a set of differently exposed panorama images. The intermediate panorama images are finally fused via a state-of-the-art multi-scale exposure fusion (MEF) algorithm to produce the final panorama image. Extensive experiments indicate that the proposed WHA algorithm significantly surpasses the related state-of-the-art color mapping methods. The proposed high dynamic range (HDR) stitching algorithm based on MEF also preserves details in the brightest and darkest regions of the input images well. The related materials will be publicly accessible at <https://github.com/yilun-xu/WHA> for reproducible research.

Index Terms—Image stitching, color mapping, weighted histogram averaging, multi-scale exposure fusion.

I. INTRODUCTION

Panorama is a visual representation of the environment viewed from one 3D position. Since the field of view (FoV) of mobile phones or digital cameras is very limited, a panorama image is often obtained by stitching a series of still sub-images which cover certain areas of the scene [1]. Lighting conditions in different areas are often different for a scene, especially an outdoor scene. If the sub-images are all shot with similar exposures, the limited dynamic range of the camera makes the panorama images lose a lot of information in the brightest or darkest areas [2]. The exposures are thus flexibly adjusted according to the lighting conditions when shooting different areas such that the generated panorama images can record richer scene information [3]. The resultant sub-images are differently exposed low dynamic range (LDR) images.

The existing high dynamic range (HDR) stitching algorithms [3], [5], [6] used the camera response function to map the LDR image to the HDR irradiance map for processing, and then tone-mapped [7] the synthesized HDR panorama image into a high-quality LDR panorama image to match the

* Corresponding author: Weihai Chen.

Yilun Xu and Weihai Chen are with the School of Automation Science and Electrical Engineering, Beihang University, Beijing, 100191 (e-mail: yilunxu_buaa@163.com, and whchen@buaa.edu.cn).

Zhengguo Li is with SRO Department, Institute for Infocomm Research, 1 Fusionopolis Way, Singapore (email: ezgli@i2r.a-star.edu.sg).

Changyun Wen is with the School of Electrical and Electronics Engineering, Nanyang Technological University, Singapore (email: ecywen@ntu.edu.sg).

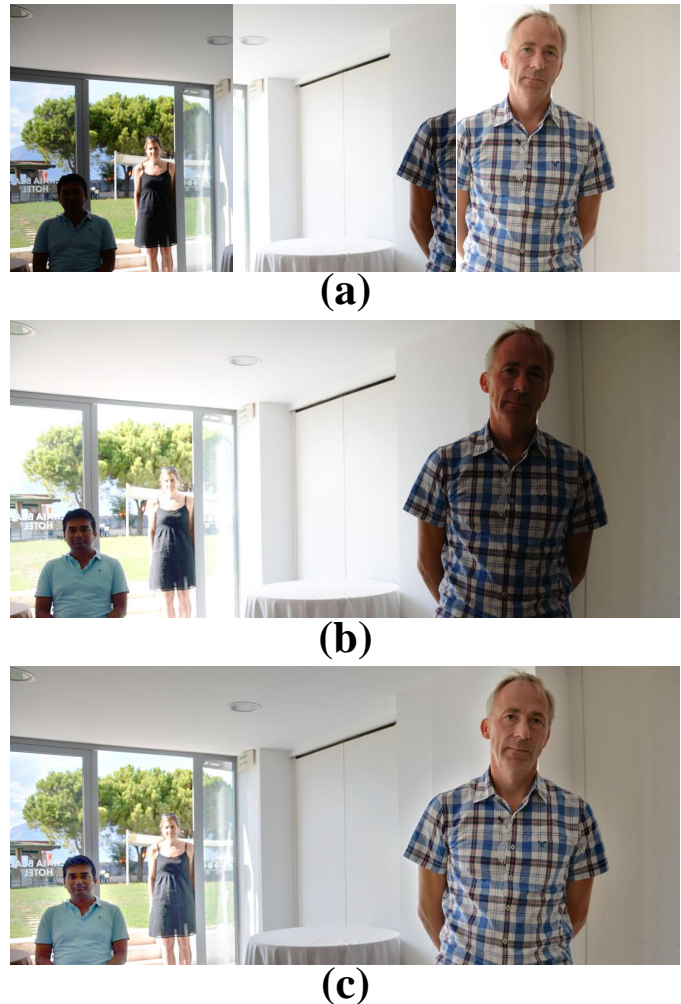


Fig. 1. An example of HDR panorama stitching result based on the MEF. (a) Input images with different exposures, (b) A panorama image aligned to the medium brightness image, (c) The HDR panorama image obtained by fusing three panorama images with different exposures through the MEF. The images come from the HDR-SICE dataset [4].

dynamic range of the display. In recent years, multi-exposure image fusion (MEF) algorithms were proposed to improve the computational efficiency and convenience of HDR imaging [8]–[11]. The algorithms can directly obtain high-quality LDR images for displays by weighting fusion of the LDR images. It can simplify the pipeline and get rid of the restriction from the lighting condition and devices. It is thus desired to develop a simpler HDR stitching algorithm than the algorithms in [3], [5], [6] by using the existing MEF algorithms. An example is shown in Fig. 1. Details in the brightest and darkest regions

are preserved much better in the Fig. 1(c).

In this paper, a novel HDR stitching algorithm is proposed by introducing a histogram bins-based color mapping algorithm. The proposed color mapping algorithm includes estimation and correction of color mapping functions (CMFs). The proposed CMFs estimation method is inspired by two methods in [2], [12]. Two steps of the method in [12] are to 1) set up a pixel level correspondence between the two differently exposed images, and 2) average over all the corresponding pixels in the other image. Unfortunately, although the method in [12] has high accuracy, the pixel level correspondence is not robust to camera movement and moving objects. The method in [2] shows that using histograms and the non-decreasing property of the CMFs to establish correspondences will be more robust to movement. Combining the advantages of the above two methods, a robust histogram bin level correspondence is built up between the two differently exposed images. Each bin in the histogram of one image thus corresponds to one unique segment in the accumulated histogram of the other image. Similar to the method in [12], the mapped value is defined as the average of intensities in the matched segment. Moreover, the estimated CMFs need to be further corrected so as to cover the whole dynamic range. Since the overlapping area of the sub-image does not necessarily contain all the pixel values in the dynamic range, the calculated CMFs will contain some empty values. The linear interpolation and extrapolation are used to fill in the empty values after the CMFs are estimated.

Instead of correcting all the sub-images using the CMFs to directly produce the final panorama image as in [13], a set of differently exposed panorama images are synthesized by using the CMFs. The brightness of each sub-image is selected as a benchmark, and the brightness of the remaining sub-images is calibrated using the proposed CMFs. All the corrected sub-images are stitched together to form an LDR panorama image. By continuously changing the benchmark sub-image, the differently exposed LDR panorama images can be obtained. The CMFs can effectively prevent the brightness distortion from appearing in the differently exposed LDR panorama images [14]. The MEF algorithm in [15] is finally adopted to fuse all the differently exposed panorama images because the experimental results in [4] show that the MEF algorithm adopted outperforms other MEF algorithms from the MEF-SSIM point of view [16]. Details in the brightest and darkest regions of the input images are well preserved by the proposed stitching algorithm. Experimental results validate the proposed algorithms. Overall, two main contributions of this paper are: 1) a novel CMF estimation algorithm which outperforms the classical algorithms in [2], [12]; and 2) a simpler HDR stitching algorithm than the algorithms in [3], [5], [6].

The rest of this paper is organized as follows. Relevant works are reviewed in Section II. Details of the proposed algorithm are presented in Section III. Extensive experimental results are provided in Section V. Lastly, concluding remarks are listed in Section VI.

II. RELATED WORKS

Relevant works on color mapping are first summarized, and details on the two most relevant color mapping algorithms are then highlighted in this section.

A. Existing Color Mapping Algorithms

Due to the limited FoV of mobile phone or digital camera, a set of still sub-images which cover certain areas of the scene is captured and stitched together to produce a panorama image [1]. Exposure of all the sub-images are usually differently because of differently covered areas, especially for those sub-images with large camera movements [17]. Due to the different exposures, there could be large intensity changes among differently exposed sub-images [8], [15]. Color mapping algorithms are usually applied to normalize all the sub-images before they are stitched together.

Many color matching algorithms have been proposed in a dozen years [2], [12], [13], [18] because they have broad application in many fields such as panorama stitching, image fusion, video color mapping, etc [19], [20]. Color mapping algorithms can be divided into model-based parametric algorithms and statistics-based non-parametric algorithms [20]. The model-based parametric algorithms assume that the color mapping from the original image to the target image follows a known mapping model. The statistics-based non-parametric algorithms do not build an explicit mapping model but estimate the look-up table from the relevant statistics of the original image and target image, and then use the look-up table as CMFs to calibrate the image.

Among the model-based parametric algorithms, the color mapping algorithm in [21] rearranges the color distribution of the source image so that the mean and variance of the original image and the target image are consistent. In order to decorrelate color channels, color space is converted into the $l\alpha\beta$ space representation so that the transformation can be applied the transformation on the special space. The gain compensation algorithm is introduced in [22] to address symmetric color balancing by a least-square minimization and is widely used in panoramic stitching tasks. The affine mapping algorithm in [23] uses probabilistic moving least squares to solve for a fully nonlinear and nonparametric color mapping in the 3D RGB color space. When images come from entirely different domains, model-based parametric algorithms will lack a certain degree of versatility and convenience, and statistics-based non-parametric algorithms may be more appropriate [19]. Accuracy of the model-based parametric algorithms could be an issue even though they are simple.

Many statistics-based non-parametric algorithms have been proposed to estimate the look-up table as CMFs. The color mapping algorithm based on the camera response functions [24] is widely used in HDR imaging [10], [25]. The camera response functions which are calculated by a sequence of multiple exposure images and camera parameters can be used to calibrate the brightness of the images. Algorithms based on truncated Gaussian models [26] and algorithms based on spline models [27], [28] are proposed to estimate the CMFs from overlapping regions. The algorithm in [2] estimates the CMFs

by matching the cumulative histogram of two images. They can be applied for image stitching, removing ghosting artifacts [29], etc. A color mapping algorithm is proposed in [13] to improve the cumulative histogram-based algorithm by using hybrid histogram matching, and it achieves state-of-the-art (SOTA) performance in the multi-camera color mapping. But when the exposure differences among the input images become large, the performance of the algorithm in [13] will drop. An algorithm is proposed in [12] for inpainting of differently exposed images. The algorithm uses geometrical correspondence between images to calculate the CMFs. The accuracy of the algorithm in [12] is higher than the algorithms in [2], [13] for two perfectly aligned images. However, when there is camera movement between two images, the accuracy of the algorithm in [12] will drop significantly. The accuracy is also an issue when there are moving objects. A new statistics-based non-parametric CMF estimation method will be proposed to overcome these problems. Same as the existing statistics-based non-parametric algorithms, the proposed algorithm has high accuracy.

B. Two Most Relevant Color Mapping Algorithms

The CMFs are a characteristic of the camera and the exposures between two images. Thus, it is scene independent [2]. In this subsection, the details of the two most relevant works [2], [12] on the estimation of CMFs are provided in order to facilitate readers to better understand the new algorithm in Section III. The CMFs are calculated in the RGB color space. Here, an example is shown for a single color channel, but the CMFs can be performed separately for each channel.

1) *Cumulative Histogram Based CMFs*: Let Z_i and Z_j be two differently exposed images. The pixel's position index and intensity of Z_i are denoted by p and z . $\Lambda_{i \rightarrow j}(z)$ is the CMF from the image Z_i to the image Z_j . The set of pixels with the value of z in the image Z_i , $\Omega_i(z)$ is defined as

$$\Omega_i(z) = \{p | Z_i(p) = z\}. \quad (1)$$

The CMF $\Lambda_{i \rightarrow j}^1(z)$ are estimated by using the cumulative histograms of the images Z_i and Z_j in [2]. Let $|\Omega_i(z)|$ be the cardinality of the set $\Omega_i(z)$ to represent the z th histogram bin of image Z_i . The cumulative histogram $H_i(z)$ of the image Z_i is then created by

$$H_i(z) = \sum_{k=0}^z |\Omega_i(k)|. \quad (2)$$

Finally, the function $\Lambda_{i \rightarrow j}^1(z)$ can be estimated as

$$\Lambda_{i \rightarrow j}^1(z) = \arg \min_{z'} |H_i(z) - H_j(z')|. \quad (3)$$

The method in [2] is based on the non-decreasing property of the CMFs. The CMFs estimated by this property are robust to camera movements and moving objects in the pair of images (Z_i, Z_j). Although the formula (3) can accurately calculate the mapping relationship between two images with similar exposure ratios, when Z_i and Z_j have a larger exposure ratio, there will be obvious mapping from one value to multiple values or from multiple values to one value. Clearly, the accuracy of the estimated CMFs by the formula (3) is an issue.

2) *Geometrical Correspondence Based CMFs*: The estimation method in [12] is based on two assumptions: 1) the images Z_i and Z_j are aligned, and 2) there is no moving object in the two images. This algorithm estimates the CMFs by 1) finding all pixels with the same intensity in one image, and 2) calculating the average of all the co-located pixels in the other image. In other words, the function $\Lambda_{i \rightarrow j}^2(z)$ is estimated as

$$\Lambda_{i \rightarrow j}^2(z) = \frac{\sum_{p \in \Omega_i(z)} Z_j(p)}{|\Omega_i(z)|}, \quad |\Omega_i(z)| \neq 0. \quad (4)$$

When Z_i does not span the whole dynamic range, that is, when $H_i(z) = 0$, there will be an 'empty value' problem. The corrected process is divided into two steps. First, a median filter is adopted starting from the middle of the valid values towards left and right separately. The second step extends two ends of the curve by using the neighbourhood slope.

It can be easily verified that $\Lambda_{i \rightarrow j}^2(z)$ is actually obtained by solving the following optimization problem:

$$\arg \min_{z'} \sum_{p \in \Omega_i(z)} (z' - Z_j(p))^2. \quad (5)$$

According to the proof, if only the CMFs is performed on image Z_i , the PSNR will be maximized by $\Lambda_{i \rightarrow j}^2(z)$.

In Formula (4), the CMFs are estimated by averaging over all the corresponding pixels in the image Z_j , this results in CMFs having sufficient accuracy for any exposure ratio between the images Z_i and Z_j . However, the function of the two assumptions used in [12] is to build up a geometrical correspondence between pixels in the two differently exposed images, the pixel level correspondence is not true if there are moving objects and camera movement in the two differently exposed images. The robustness of this method with respect to camera movement and/or moving objects is thus an issue.

III. THE PROPOSED CMF ESTIMATION METHOD

In this section, a novel color mapping algorithm that inherits the advantages of [2], [12] is introduced in this section.

A. Initial Estimation of CMF via WHA

This new method uses the correspondence among the histogram bins rather than among the geometrical correspondence of the two differently exposed images. The correspondence among the histogram bins of the images Z_i and Z_j can be built up by using the non-decreasing property of the CMFs.

Consider two pixels $Z_i(p)$ and $Z_i(p')$ which satisfy $Z_i(p) > Z_i(p')$. The bins in the image Z_j corresponding to $Z_i(p)$ and $Z_i(p')$ are $|\Omega_j(z)|$ and $|\Omega_j(z')|$, respectively. Since the CMF is non-decreasing, z is not smaller than z' . Such a property is utilized to find all the sub-bins (or bins) in the image Z_j corresponding to the bin $|\Omega_i(z)|$.

A non-decreasing mapping function $\psi_{i \rightarrow j}(z)$ is defined as

$$H_j(\psi_{i \rightarrow j}(z) - 1) < H_i(z) \leq H_j(\psi_{i \rightarrow j}(z)), \quad (6)$$

and $\psi_{i \rightarrow j}(-1)$ is 0. According to the definitions of $H_i(z)$ and $H_j(z)$, $|\Omega_j(\psi_{i \rightarrow j}(z - 1))|$ and $|\Omega_j(\psi_{i \rightarrow j}(z))|$ are the first and last bins corresponding to the bin $|\Omega_i(z)|$, respectively. The above correspondence among the histogram bins is also true

for the two differently exposed images with camera movement and moving objects.

Let the sizes of sub-bins (or bins) in the image Z_j corresponding to the bin $|\Omega_i(z)|$ be denoted by $\hat{H}_{i \rightarrow j}^z(k)$, and it is defined as in the following two cases:

Case 1: $\psi_{i \rightarrow j}(z-1) < \psi_{i \rightarrow j}(z)$. $\hat{H}_{i \rightarrow j}^z(k)$ is defined as

$$\hat{H}_{i \rightarrow j}^z(k) = \begin{cases} H_j(k) - H_i(z-1), & \text{if } k = \psi_{i \rightarrow j}(z-1) \\ H_i(z) - H_j(k-1), & \text{if } k = \psi_{i \rightarrow j}(z) \\ H_j(k) - H_j(k-1), & \text{otherwise} \end{cases} \quad (7)$$

Case 2: $\psi_{i \rightarrow j}(z-1) = \psi_{i \rightarrow j}(z)$. $\hat{H}_{i \rightarrow j}^z(k)$ is defined as

$$\hat{H}_{i \rightarrow j}^z(k) = H_i(z) - H_i(z-1). \quad (8)$$

It can be easily verified that

$$\sum_{k=\psi_{i \rightarrow j}(z-1)}^{\psi_{i \rightarrow j}(z)} \hat{H}_{i \rightarrow j}^z(k) = |\Omega_i(z)|. \quad (9)$$

By using the correspondence among the histogram bins, the proposed CMF $\Lambda_{i \rightarrow j}(z)$ is then defined as

$$\Lambda_{i \rightarrow j}(z) = \frac{\sum_{k=\psi_{i \rightarrow j}(z-1)}^{\psi_{i \rightarrow j}(z)} k \hat{H}_{i \rightarrow j}^z(k)}{|\Omega_i(z)|}, \quad |\Omega_i(z)| \neq 0. \quad (10)$$

The difference between the proposed CMF and the CMF in the equation (3) is presented as follows

Let z'^* be defined as

$$z'^* = \arg \min_{z' \in \{\psi_{i \rightarrow j}(z)-1, \psi_{i \rightarrow j}(z)\}} \{|H_i(z) - H_j(z')|\}. \quad (11)$$

It can be derived from the equations (3), (6), (9), and (11) that

$$\Lambda_{i \rightarrow j}^1(z) = \frac{\sum_{k=\psi_{i \rightarrow j}(z-1)}^{\psi_{i \rightarrow j}(z)} z'^* \hat{H}_{i \rightarrow j}^z(k)}{|\Omega_i(z)|}, \quad |\Omega_i(z)| \neq 0. \quad (12)$$

Clearly, k in the equation (10) is replaced by z'^* in the equation (12). Similar to the formula (4), the proposed averaging method has higher accuracy for any exposure ratio than formula (3). In addition, compared with $Z_j(p)$ in formula (4), the change of $\hat{H}_{i \rightarrow j}^z(k)$ in formula (10) is not sensitive to movement of camera and objects, so the proposed algorithm is more robust than formula (4). In general, this new method is more accurate than [2] and more robust than [12].

B. Interpolation and Extrapolation of the Proposed CMF

Since the image Z_i does not necessarily include pixels in all the dynamic range, there is often a problem of empty bins. When $|\Omega_i(z)| = 0$, the function $\Lambda_{i \rightarrow j}(z)$ can be calculated by using two neighboring $\Lambda_{i \rightarrow j}(z_1)$ and $\Lambda_{i \rightarrow j}(z_2)$, and the formula is given as follows:

$$\Lambda_{i \rightarrow j}(z) = \frac{(z - z_1)(\Lambda_{i \rightarrow j}(z_1) - \Lambda_{i \rightarrow j}(z_2))}{z_1 - z_2} + \Lambda_{i \rightarrow j}(z_1), \quad (13)$$

where the z_1 and z_2 can be estimated from

$$\begin{aligned} \min \quad & \{|z - z_1| + |z - z_2|\} \\ \text{s. t.} \quad & \lambda(z - z_1)(z - z_2) < 0, \\ & |\Omega_i(z_1)| |\Omega_i(z_2)| \neq 0. \end{aligned} \quad (14)$$

Here, λ is set as 1 for the interpolation, and -1 for the extrapolation.

IV. APPLICATION TO HDR PANORAMA IMAGING

Inputs of the proposed algorithm are $N (\geq 2)$ images to be stitched. Without loss of generality, consider the case that N is 3. All the three images Z_1 , Z_2 , and Z_3 have different exposures and partially overlapping areas. All the input images are supposed to be geometrically aligned. Three differently exposed panorama image $\tilde{Z}_l (l \leq l \neq 3)$ are first synthesized from the images $z_l (1 \leq l \leq 3)$. They are then fused together to produce the output \tilde{Z} .

The CMFs $\Lambda_{1 \rightarrow 2}(z)$ and $\Lambda_{2 \rightarrow 1}(z)$ as well as $\Lambda_{2 \rightarrow 3}(z)$ and $\Lambda_{3 \rightarrow 2}(z)$ are estimated from the two successive images' overlapping area. Three differently exposed panorama images are synthesized as below.

1) Taking the brightness of Z_1 as the benchmark, the images obtained by calibrating the images Z_2 and Z_3 are denoted as $Z_{2 \rightarrow 1}$ and $Z_{3 \rightarrow 1}$. They are calculated as

$$\begin{cases} Z_{2 \rightarrow 1} = \Lambda_{2 \rightarrow 1}(Z_2) \\ Z_{3 \rightarrow 1} = \Lambda_{3 \rightarrow 1}(Z_3) \end{cases}, \quad (15)$$

where the CMF $\Lambda_{3 \rightarrow 1}(z)$ is

$$\Lambda_{3 \rightarrow 1}(z) = \Lambda_{2 \rightarrow 1}(\hat{\Lambda}_{3 \rightarrow 2}(z)). \quad (16)$$

The first intermediate panorama image, \tilde{Z}_1 , is obtained by stitching all the images Z_1 , $Z_{2 \rightarrow 1}$, and $Z_{3 \rightarrow 1}$. The brightness of the image \tilde{Z}_1 is same as that of the image Z_1 .

2) Taking the brightness of Z_2 as the benchmark, the images obtained by calibrating the image Z_1 and Z_3 are denoted as $Z_{1 \rightarrow 2}$ and $Z_{3 \rightarrow 2}$. They are computed as

$$\begin{cases} Z_{1 \rightarrow 2} = \Lambda_{1 \rightarrow 2}(Z_1) \\ Z_{3 \rightarrow 2} = \Lambda_{3 \rightarrow 2}(Z_3) \end{cases}. \quad (17)$$

The second intermediate panorama image, \tilde{Z}_2 , is obtained by stitching all the images $Z_{1 \rightarrow 2}$, Z_2 , and $Z_{3 \rightarrow 2}$. The brightness of the image \tilde{Z}_2 is same as that of the image Z_2 .

3) Taking the brightness of Z_3 as the benchmark, the images obtained by calibrating the images Z_1 and Z_2 are denoted as $Z_{1 \rightarrow 3}$ and $Z_{2 \rightarrow 3}$. They are calculated as

$$\begin{cases} Z_{1 \rightarrow 3} = \Lambda_{1 \rightarrow 3}(Z_1) \\ Z_{2 \rightarrow 3} = \Lambda_{2 \rightarrow 3}(Z_2) \end{cases}, \quad (18)$$

where the CMF $\Lambda_{1 \rightarrow 3}(z)$ is computed as

$$\Lambda_{1 \rightarrow 3}(z) = \Lambda_{2 \rightarrow 3}(\Lambda_{1 \rightarrow 2}(z)). \quad (19)$$

The third intermediate panorama image, \tilde{Z}_3 , is obtained by stitching all the images $Z_{1 \rightarrow 3}$, $Z_{2 \rightarrow 3}$, and Z_3 . The brightness of the image \tilde{Z}_3 is same as that of the image Z_3 .

The final panorama image \tilde{Z} can be obtained by fusing all the three differently exposed panorama images \tilde{Z}_1 , \tilde{Z}_2 , and \tilde{Z}_3 through the MEF algorithm in [15]. It was shown in

[4] that the MEF algorithm in [15] outperforms other MEF algorithms from the MEF-SSIM point of view [16]. Details in the brightest and darkest regions of the three images Z_1 , Z_2 and Z_3 are preserved well in the panorama image \hat{Z} .

V. EXPERIMENT RESULTS

Extensive experimental results are provided to verified the proposal algorithms. Readers are invited to view to electronic version of figures and zoom in them so as to better appreciate differences among all images.

A. Implementation Details

1) *Dataset Description*: Experiments are conducted on two datasets, VETHDR-Nikon dataset and HDR-SICE dataset. Between them, the VETHDR-Nikon dataset is used to evaluate the performance of CMFs, and the HDR-SICE dataset is used to show the results of the MEF-based HDR stitching algorithm.

The VETHDR-Nikon dataset is from [30], collected by a Nikon 7200 camera. It consists of 495 pairs of images in 8-bit JPEG files format. Each pair consists of two full-resolution images, with long and short exposure times, respectively. The exposure time ratio and ISO are fixed as 8 and 800, during shooting respectively. All the images are resized to 1000×1600 . Camera shaking, object movement are strictly controlled to ensure that only the illumination is changed.

The HDR-SICE dataset is from [31], collected by 7 different models of cameras. It includes 589 sequences from indoor and outdoor scenes, containing a total number of 4, 413 multiexposure images. All the images are resized to 480×1080 . The multiple sequences with EV shifted by $\pm(0.5, 0.7, 1.0, 2.0, 3.0)$ are well-aligned. In each image sequence, we first select three images with different exposures and then crop 480×400 size images from different positions of the three images as input. The size of the overlap area between the input adjacent images is 720×60 .

2) *CMFs Comparison Description*: In the VETHDR-Nikon dataset, the overlapping areas in each pair of images are well-aligned. However, in actual situations, since the shooting angles of the two images to be stitched are different, the overlapping areas are always not well-aligned. In order to simulate the real situation of the overlapping area, Fig. 2 shows how to process the input image. Specifically, the N_c columns of pixels on the left and N_c rows of pixels on the bottom of the image (a) are cut off, the N_c columns of pixels on the right and N_c rows of pixels on the top of the image (b) are also cut off. The remaining areas are used as the simulated overlap area. CMFs are first estimated by the simulated overlap areas and then used to correct the brightness of image (a) or (b).

Moreover, in order to test the CMFs more comprehensively, each pair of images in the VETHDR-Nikon dataset will be tested twice. Specifically, use the dark image as the reference to correct the bright image, and then use the bright image as the reference to correct the dark image. So each CMFs algorithm will be tested 990 times on the VETHDR-Nikon dataset.

In terms of quantitative comparison, we choose PSNR, SSIM, FSIM, iCID and running time as the evaluation metrics.

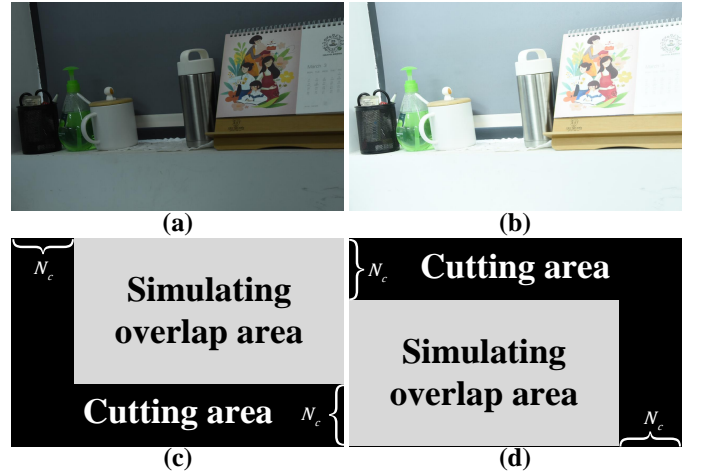


Fig. 2. An example of simulating overlapping areas. (a) and (b) are the input image pairs, (c) and (d) show the way to simulate the overlapping area of (a) and (b), respectively.

All results are tested on a laptop with Intel Core i7-9750H CPU 2. 59GHz, 32. 0 GB memory and Matlab R2019a installed. The all evaluation metrics are explained as follows:

- **PSNR**: Peak signal-to-noise ratio, the higher score comes with the better performance.
- **SSIM**: Structural similarity [32], the higher score comes with the better performance.
- **FSIM**: Feature similarity [33], the higher score comes with the better performance.
- **iCID**: Improved color image difference [34], the lower score comes with the better performance.
- **Time**: The time it takes for the CMFs algorithm to map a image, it does not include the time to read and save the image.

B. Robustness and Accuracy Analysis

In order to verify that the WHA algorithm can inherit the high robustness of the CHM algorithm [2] and the high accuracy of the CG algorithm [12], the three algorithms are compared in different situations quantitatively. Specifically, when using the simulated overlap area to estimate the CMFs, the value of N_c is changed to simulate the different degrees of misalignment between the overlap areas. The larger N_c , the greater the degree of misalignment in the overlapping area. Note that when $N_c = 0$, because the empty value problem in the CG algorithm will not affect the accuracy, there is no need to use the corrected process in section II-B2. When $N_c \neq 0$, the corrected process will be used.

The quantitative comparison results are shown in Table I. It can be seen that when the overlapping area is well aligned ($N_c = 0$), the accuracy of CG is the highest, and the accuracy of CHM is the lowest, but the accuracy of the WHA is very close to that of CG. This shows that the WHA has inherited the high precision of the CG well. When the degree of misalignment in the overlapping area becomes larger ($N_c \uparrow$), the sensitivity of CG to misalignment causes the accuracy to drop quickly, but the accuracy of the WHA and

TABLE I

QUANTITATIVE COMPARISON AMONG THE CHM, GC AND THE PROPOSED WHA IN DIFFERENT NUMBERS OF OFFSET PIXELS. THE BEST RESULTS ARE SHOWN IN BOLD, AND THE SECOND-BEST RESULTS ARE SHOWN IN RED. THE RESULTS COME FROM THE VETHDR-NIKON DATASET.

N_c	PSNR \uparrow			SSIM \uparrow			FSIM \uparrow			iCID(%) \downarrow		
	WHA	CHM	GC	WHA	CHM	GC	WHA	CHM	GC	WHA	CHM	GC
0	34.54	32.49	34.83	0.9156	0.9032	0.9210	0.9817	0.9743	0.9814	4.70	7.04	4.45
2	34.53	32.48	31.82	0.9156	0.9032	0.9041	0.9817	0.9743	0.9714	4.70	7.04	7.01
4	34.51	32.46	30.45	0.9156	0.9031	0.8927	0.9817	0.9743	0.9619	4.71	7.05	8.54
6	34.47	32.43	29.54	0.9155	0.9031	0.8849	0.9816	0.9742	0.9546	4.73	7.06	9.70
8	34.43	32.40	28.87	0.9154	0.9030	0.8774	0.9816	0.9741	0.9467	4.75	7.08	10.83
10	34.38	32.36	28.17	0.9153	0.9029	0.8693	0.9815	0.9740	0.9385	4.77	7.10	11.98
12	34.32	32.31	27.64	0.9152	0.9027	0.8622	0.9814	0.9739	0.9314	4.79	7.13	12.99
14	34.25	32.25	27.24	0.9150	0.9025	0.8571	0.9812	0.9738	0.9258	4.82	7.16	13.79
16	34.18	32.20	26.87	0.9148	0.9024	0.8514	0.9811	0.9737	0.9196	4.86	7.19	14.64

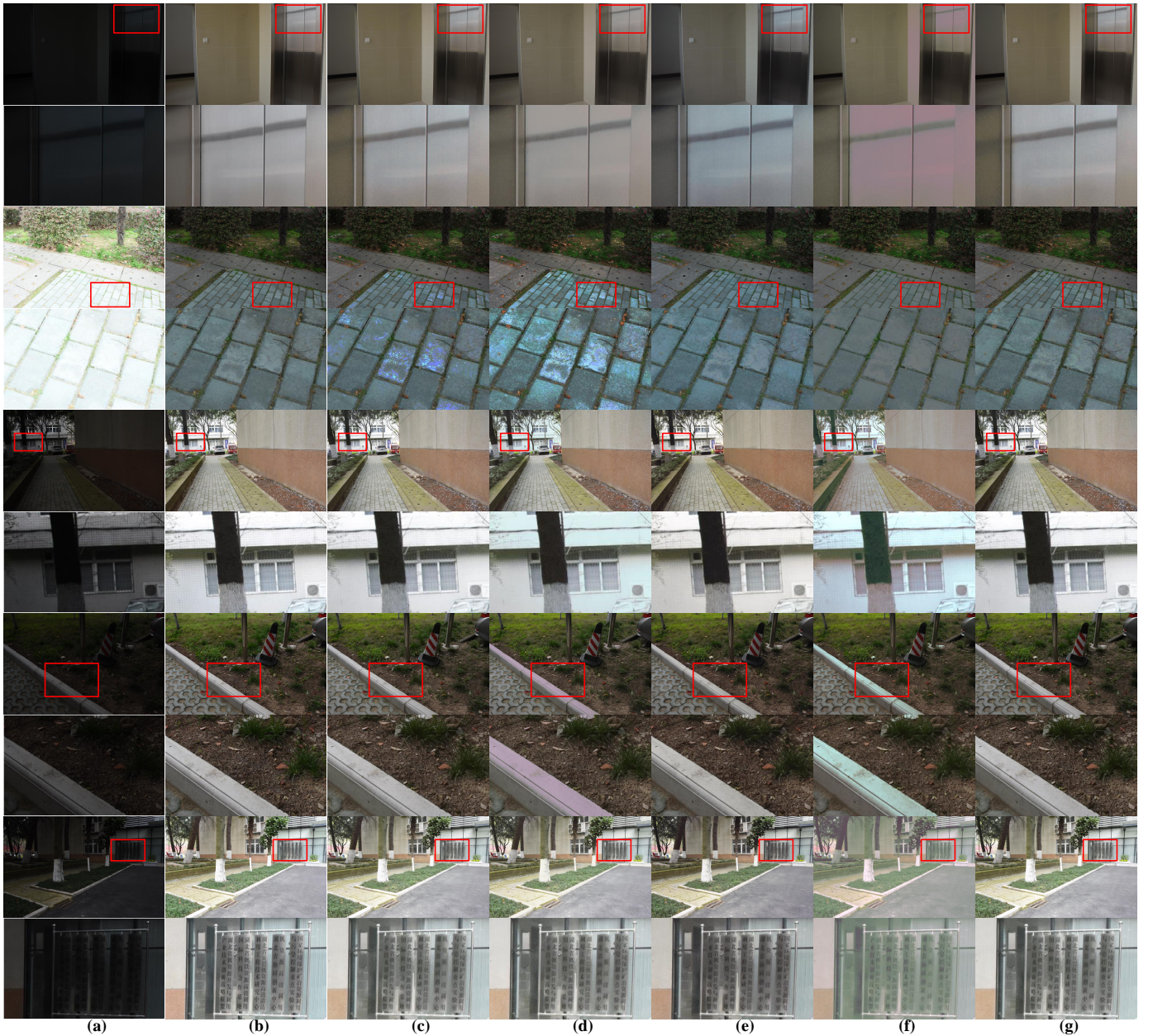


Fig. 3. Qualitative comparison among the existing CMFs' algorithms and the proposed WHA. (a) Original Images, (b) Ground truth, (c) CHM, (d) HHM, (e) PCRF, (f) GPS, (g) WHA. The results come from the VETHDR-Nikon dataset.

CHM only drops a little bit. This shows that the WHA also inherits the robustness of the CHM against dislocation. As the WHA inherits the advantages of the CG and CHM, the WHA maintains the highest accuracy in the case of non-alignment ($N_c \neq 0$).

C. Comparison with Existing CMFs' Algorithms

The proposed WHA algorithm is compared with eight existing CMFs algorithms [2], [10], [12], [13], [23], [26]–[28] qualitatively and quantitatively on the VETHDR-Nikon dataset. Table II gives a brief technical summary of these algorithms.

TABLE II
A BRIEF SUMMARY OF CMFS ALGORITHMS.

Method	Summary Description
CHM [2]	using cumulative histogram
GC [12]	using geometric correspondence between pixels
HHM [13]	using hybrid histogram matching algorithm
PCRF [10]	using prior information about camera response function
TG [26]	using histogram simulated by truncated Gaussians
AM [23]	using affine map
3MS [27]	using monotonic splines and three-channel correlation
GPS [28]	using gradient preserving spline
WHA	using weighted histogram averaging algorithm

N_c is set to 10 in order to verify the accuracy and robustness of the CMFs algorithm simultaneously. The results about 5 evaluation metrics are reported in Table III. With the second fastest running speed, our method achieves the best performance in all the PSNR, SSIM, FSIM, and iCID. This strongly proves that the proposed WHA algorithm has the elegant characteristics of high precision and high robustness.

TABLE III
QUANTITATIVE COMPARISON AMONG THE EXISTING CMFS' ALGORITHMS. THE BEST RESULTS ARE SHOWN IN BOLD, AND THE SECOND-BEST RESULTS ARE SHOWN IN RED.

Method	PSNR \uparrow	SSIM \uparrow	FSIM \uparrow	iCID(%) \downarrow	Time(s) \downarrow
HHM [13]	29.88	0.8977	0.9673	8.24	0.11
PCRF [10]	30.69	0.9056	0.9715	7.67	1.79
TG [26]	29.34	0.8897	0.9391	11.35	12.52
AM [23]	25.68	0.8413	0.8882	18.49	0.54
3MS [27]	28.96	0.8857	0.9455	11.17	7.70
GPS [28]	30.96	0.8945	0.9643	9.36	151.09
GC [12]	28.17	0.8693	0.9385	11.98	1.77
CHM [2]	32.36	0.9029	0.9740	7.10	0.08
WHA	34.38	0.9153	0.9815	4.77	0.08

For a qualitative comparison, several representative methods were selected. The visualization results and their detailed parts are shown in Fig. 3. In the first row, the color of the door is mapped incorrectly in (d), (e) and (f). In the second row, the luminance of images in (d) and (f) is different from the ground-truth, and the color of images in (c), (e) and (f) is abnormal. In a nutshell, the results in (c) sometimes have abnormal color when mapped from lighter images, the results in (d), (e) and (f) are likely to have abnormal color and luminance. Different from these methods, the proposed algorithm is robust to most scenes, providing accurate results.

The overall comparison demonstrates the effectiveness of the proposed WHA algorithm.

D. Comparison of Different Stitching Methods

This subsection compares the MEF-based HDR stitching method with the traditional stitching method qualitatively, and the WHA is used to estimate the CMFs. The comparison results are shown in Figure 4.

The panorama images obtained by the traditional image stitching algorithm are usually aligned to an input image of a certain brightness, which will cause the partial loss of information from the input images. For example, the panorama image in (b) has a large overexposed area and will lose information from the brightest areas in (a). Although there are smaller overexposed and underexposed areas in the panorama image in (c), the information from the brightest and darkest areas in (a) will still be lost. The panorama image in (d) has a large underexposed area and will lose information from the darkest area in (a). Clearly, it is difficult for the traditional stitching method to preserve details in both the brightest and darkest regions of the input images simultaneously.

Since the information of a certain image in (a) will always be completely retained in a panorama image in (b), (c), or (d), by fusing the panorama images in (b), (c), and (d) with the MEF algorithm in [15], the resultant HDR panorama images should preserve information better. It can be shown from the HDR panorama images in (e) that the overexposed and underexposed areas are significantly reduced, and the information from the brightest and darkest areas in (a) are indeed preserved much better.

VI. CONCLUSION REMARKS AND DISCUSSION

In this paper, a novel color mapping estimation algorithm is proposed by introducing a new concept of weighted histogram averaging (WHA), and it is applied to study image stitching. Instead of only correcting the color and brightness difference as in the existing image stitching algorithms, a set of differently exposed panorama images is synthesized and fused to produce the desired panorama images. Details in the brightest and darkest regions of the input images are well preserved in the panorama images.

The proposed color mapping estimation algorithm can be applied to estimate optical flows of differently exposed images, and to improve the ghost removal algorithms in [29]. It is worth noting that the proposed stitching algorithm assumes that there are no moving objects in the overlapping areas. This assumption might not be true. The improved ghost removal algorithms can be applied to study the problem. The stitched image can be further improved by using existing detail enhancement algorithms [35]. All these problems will be studied in our future research.

ACKNOWLEDGMENT

This work is supported by the National Natural Science Foundation of China under the research project 61620106012.



Fig. 4. Qualitative comparison among the different stitching results. (a) Original images with different exposure, (b) Panorama image aligned to the brightest original image, (c) Panorama image aligned to the second bright original image, (d) Panorama aligned to the third bright original image, (e) The HDR panorama image obtained by fusing three panorama images with different brightness through the MEF algorithm. The results come from the HDR-SICE dataset.

REFERENCES

- [1] M. Brown, D. G. Lowe *et al.*, "Recognising panoramas." in *ICCV*, vol. 3, 2003, p. 1218.
- [2] M. D. Grossberg and S. K. Nayar, "Determining the camera response from images: What is knowable?" *IEEE Transactions on pattern analysis and machine intelligence*, vol. 25, no. 11, pp. 1455–1467, 2003.
- [3] A. Eden, M. Uyttendaele, and R. Szeliski, "Seamless image stitching of scenes with large motions and exposure differences," in *2006 IEEE Computer Society Conference on Computer Vision and Pattern Recognition (CVPR'06)*, vol. 2. IEEE, 2006, pp. 2498–2505.
- [4] J. Cai, S. Gu, and L. Zhang, "Learning a deep single image contrast enhancer from multi-exposure images," *IEEE Transactions on Image Processing*, vol. 27, no. 4, pp. 2049–2062, 2018.
- [5] P. Ostiak, "Implementation of hdr panorama stitching algorithm," in *Proceedings of the 10th CESC Conference*. Citeseer, 2006, pp. 24–26.
- [6] V. Popovic, K. Seyid, E. Pignat, Ö. Çoğal, and Y. Leblebici, "Multi-camera platform for panoramic real-time hdr video construction and rendering," *Journal of Real-Time Image Processing*, vol. 12, no. 4, pp. 697–708, 2016.
- [7] F. Durand and J. Dorsey, "Fast bilateral filtering for the display of high-dynamic-range images," in *Proceedings of the 29th annual conference on Computer graphics and interactive techniques*, 2002, pp. 257–266.
- [8] T. Mertens, J. Kautz, and F. Van Reeth, "Exposure fusion: A simple and practical alternative to high dynamic range photography," in *Computer graphics forum*, vol. 28, no. 1. Wiley Online Library, 2009, pp. 161–171.
- [9] Z. Li, Z. Wei, C. Wen, and J. Zheng, "Detail-enhanced multi-scale exposure fusion," *IEEE Transactions on Image processing*, vol. 26, no. 3, pp. 1243–1252, 2017.
- [10] Y. Yang, W. Cao, S. Wu, and Z. Li, "Multi-scale fusion of two large-exposure-ratio images," *IEEE Signal Processing Letters*, vol. 25, no. 12, pp. 1885–1889, 2018.
- [11] F. Kou, Z. Wei, W. Chen, X. Wu, C. Wen, and Z. Li, "Intelligent detail enhancement for exposure fusion," *IEEE Transactions on Multimedia*, vol. 20, no. 2, pp. 484–495, 2018.
- [12] Z. Zhu, Z. Li, S. Rahardja, and P. Fränti, "Recovering real-world scene: high-quality image inpainting using multi-exposed references," *Electronics Letters*, vol. 45, no. 25, pp. 1310–1312, 2009.
- [13] C. Ding and Z. Ma, "Multi-camera color correction via hybrid histogram matching," *IEEE Transactions on Circuits and Systems for Video Technology*, 2020.
- [14] Y. Ren, Z. Ying, T. H. Li, and G. Li, "LEARM: Low-light image enhancement using camera response model," *IEEE Transactions on Circuits and Systems for Video Technology*, vol. 29, no. 4, pp. 968–981, 2019.
- [15] F. Kou, Z. Li, C. Wen, and W. Chen, "Multi-scale exposure fusion via gradient domain guided image filtering," in *IEEE International Conference on Multimedia and Expo*, 2017, pp. 1105–1110.
- [16] K. Ma, K. Zeng, and Z. Wang, "Perceptual quality assessment for multi-exposure image fusion," *IEEE Transactions on Image Processing*, vol. 24, no. 11, pp. 3345–3356, 2015.
- [17] E. Reinhard, W. Heidrich, P. Debevec, S. Pattanaik, G. Ward, and K. Myszkowski, *High dynamic range imaging: acquisition, display, and image-based lighting*. Morgan Kaufmann, 2010.
- [18] F. Bellavia and C. Colombo, "Dissecting and reassembling color correction algorithms for image stitching," *IEEE Transactions on Image Processing*, vol. 27, no. 2, pp. 735–748, 2017.

- [19] H. S. Faridul, T. Pouli, C. Chamaret, J. Stauder, E. Reinhard, D. Kuzovkin, and A. Trémeau, "Colour mapping: A review of recent methods, extensions and applications," in *Computer Graphics Forum*, vol. 35, no. 1. Wiley Online Library, 2016, pp. 59–88.
- [20] W. Xu and J. Mulligan, "Performance evaluation of color correction approaches for automatic multi-view image and video stitching," in *2010 IEEE Computer Society Conference on Computer Vision and Pattern Recognition*. IEEE, 2010, pp. 263–270.
- [21] E. Reinhard, M. Adhikhmin, B. Gooch, and P. Shirley, "Color transfer between images," *IEEE Computer graphics and applications*, vol. 21, no. 5, pp. 34–41, 2001.
- [22] M. Brown and D. G. Lowe, "Automatic panoramic image stitching using invariant features," *International journal of computer vision*, vol. 74, no. 1, pp. 59–73, 2007.
- [23] Y. Hwang, J.-Y. Lee, I. So Kweon, and S. Joo Kim, "Color transfer using probabilistic moving least squares," in *Proceedings of the IEEE conference on computer vision and pattern recognition*, 2014, pp. 3342–3349.
- [24] P. E. Debevec and J. Malik, "Recovering high dynamic range radiance maps from photographs," in *Conference on Computer Graphics & Interactive Techniques*, 1997, pp. 369–378.
- [25] C. Zheng, Z. Li, Y. Yang, and S. Wu, "Single image brightening via multi-scale exposure fusion with hybrid learning," *IEEE Transactions on Circuits and Systems for Video Technology*, vol. 31, no. 4, pp. 1425–1435, 2020.
- [26] M. Oliveira, A. D. Sappa, and V. Santos, "A probabilistic approach for color correction in image mosaicking applications," *IEEE Transactions on image Processing*, vol. 24, no. 2, pp. 508–523, 2014.
- [27] H. Faridul, J. Stauder, J. Kervec, and A. Trémeau, "Approximate cross channel color mapping from sparse color correspondences," in *Proceedings of the IEEE international conference on computer vision workshops*, 2013, pp. 860–867.
- [28] F. Bellavia and C. Colombo, "Dissecting and reassembling color correction algorithms for image stitching," *IEEE Transactions on Image Processing*, vol. 27, no. 2, pp. 735–748, 2017.
- [29] J. Zheng, Z. Li, Z. Zhu, S. Wu, and S. Rahardja, "Hybrid patching for a sequence of differently exposed images with moving objects," *IEEE transactions on image processing*, vol. 22, no. 12, pp. 5190–5201, 2013.
- [30] C. Zheng, Z. Li, Y. Yang, and S. Wu, "Exposure interpolation via hybrid learning," in *IEEE International Conference on Acoustics, Speech and Signal Processing*, 2020, pp. 2098–2102.
- [31] J. Cai, S. Gu, and L. Zhang, "Learning a deep single image contrast enhancer from multi-exposure images," *IEEE Transactions on Image Processing*, vol. 27, no. 4, pp. 2049–2062, 2018.
- [32] Z. Wang, A. C. Bovik, H. R. Sheikh, and E. P. Simoncelli, "Image quality assessment: from error visibility to structural similarity," *IEEE Trans. on Image Processing*, vol. 13, no. 4, pp. 600–612, 2004.
- [33] L. Zhang, L. Zhang, X. Mou, and D. Zhang, "Fsim: A feature similarity index for image quality assessment," *IEEE transactions on Image Processing*, vol. 20, no. 8, pp. 2378–2386, 2011.
- [34] J. Preiss, F. Fernandes, and P. Urban, "Color-image quality assessment: From prediction to optimization," *IEEE Transactions on Image Processing*, vol. 23, no. 3, pp. 1366–1378, 2014.
- [35] Z. Li, J. Zheng, Z. Zhu, W. Yao, and S. Wu, "Weighted guided image filtering," *IEEE Transactions on Image Processing*, vol. 24, no. 1, pp. 120–129, 2015.